



Ternary nitride semiconductors in the rocksalt crystal structure

Sage R. Bauers^{a,1}, Aaron Holder^{a,b}, Wenhao Sun^c, Celeste L. Melamed^{a,d}, Rachel Woods-Robinson^{a,c,e}, John Mangum^f, John Perkins^a, William Tumas^a, Brian Gorman^f, Adele Tamboli^a, Gerbrand Ceder^{c,g}, Stephan Lany^a, and Andriy Zakutayev^{a,1}

^aMaterials Science Center, National Renewable Energy Laboratory, Golden, CO 80401; ^bDepartment of Chemical and Biological Engineering, University of Colorado, Boulder, CO 80309; ^cMaterials Sciences Division, Lawrence Berkeley National Laboratory, Berkeley, CA 94720; ^dDepartment of Physics, Colorado School of Mines, Golden, CO 80401; ^eApplied Science and Technology Graduate Group, University of California, Berkeley, CA 94720; ^fDepartment of Metallurgical and Materials Engineering, Colorado School of Mines, Golden, CO 80401; and ^gDepartment of Materials Science and Engineering, University of California, Berkeley, CA 94720

Edited by Maw-Kuen Wu, Academia Sinica (Taiwan), Taipei, Taiwan, and approved June 7, 2019 (received for review March 21, 2019)

Inorganic nitrides with wurtzite crystal structures are well-known semiconductors used in optical and electronic devices. In contrast, rocksalt-structured nitrides are known for their superconducting and refractory properties. Breaking this dichotomy, here we report ternary nitride semiconductors with rocksalt crystal structures, remarkable electronic properties, and the general chemical formula $Mg_xTM_{1-x}N$ ($TM = Ti, Zr, Hf, Nb$). Our experiments show that these materials form over a broad metal composition range, and that Mg-rich compositions are nondegenerate semiconductors with visible-range optical absorption onsets (1.8 to 2.1 eV) and up to $100 \text{ cm}^2 \text{ V}^{-1} \text{ s}^{-1}$ electron mobility for $MgZrN_2$ grown on MgO substrates. Complementary ab initio calculations reveal that these materials have disorder-tunable optical absorption, large dielectric constants, and electronic bandgaps that are relatively insensitive to disorder. These ternary $Mg_xTM_{1-x}N$ semiconductors are also structurally compatible both with binary TMN superconductors and main-group nitride semiconductors along certain crystallographic orientations. Overall, these results highlight $Mg_xTM_{1-x}N$ as a class of materials combining the semiconducting properties of main-group wurtzite nitrides and rocksalt structure of superconducting transition-metal nitrides.

materials discovery | nitride semiconductors | defect-tolerant materials

Nitride materials are relevant to several industrial and technological fields, and historically are separated into two families. The first family is main-group metal nitride semiconductors with wurtzite crystal structure, typified by (Al, Ga, In)N, which are known for direct bandgaps and high carrier mobilities (1, 2). Over the last few decades these materials have become particularly important due to proliferation of solid-state lighting, radiofrequency transistors, and high information density optical storage media (1–3). The second family is transition-metal (TM) nitrides with rocksalt structures, such as TiN, VN, and CrN, which are often found as industrial hard coatings and diffusion barriers in semiconductor devices (4). In these compounds, the open d -shell of the TM leads to metallic behavior; many exhibit superconducting transitions approaching 20 K (5). While there are several examples of inorganic nitrides with more structural- and chemical complexity (6–9), and even some cases of semiconducting rocksalt nitrides (e.g., ScN) (10) or metallic wurtzite nitrides (e.g., $ZnMoN_2$) (11), these are exceptions to the general trends observed in the most technologically relevant materials.

In the past decade, increased attention has been devoted to semiconducting II-IV- N_2 ternaries, which are structurally similar to III-N wurtzite compounds but with the main-group III^{3+} metal replaced with group II^{2+} and group IV^{4+} metals (for example, Zn^{2+} and Ge^{4+} instead of Ga^{3+}) (12). Very recently, we expanded this materials design concept to ternary nitrides with other main-group (e.g., Sb^{5+} in Zn_2SbN_3) (13) and TM (Mo^{6+} in $ZnMo_3N_4$) (11) elements in wurtzite-derived crystal structures. However, it is not clear if a similar approach might be used in

TM nitrides with rocksalt structures. On one hand, the group IV TMs usually exist in 3+ valence states in nitrides (e.g., TiN) (14). On the other hand, introducing electropositive low-valence alkaline earth (AE) cations, such as Mg^{2+} , could move TMs into higher oxidation states, closing the d -shell and inducing semiconducting behavior (15). Furthermore, TM nitride rocksalts are already known to adopt both cation- and anion-substoichiometric defect phases (16–18), so metal site vacancies could reasonably be accommodated and possibly filled with AE cations. Even though computational studies suggest that some such compounds can be formed (19, 20), few of them have been synthesized (21–24), and reports of thin-film synthesis and functional properties are even rarer (25–28).

Here, we report a family of ternary nitride semiconductors with rocksalt structures and the general formula $Mg_{G-3}TMN_{G-2}$, where G is the group number of TM . We specifically consider the compounds $MgTiN_2$, $MgZrN_2$, $MgHfN_2$, and Mg_2NbN_3 . Ab initio calculations predict rocksalt-derived structures, where multiple cation motifs on the metal sublattice can be close in energy. They also suggest these compounds have disorder-tunable optical absorption but disorder-tolerant electronic bandgaps, low effective

Significance

Inorganic nitrides are important technological materials, many of which belong to one of two families: hexagonal main-group metal nitride semiconductors and cubic transition-metal nitride superconductors ($TMNs$). This mixed experimental and theoretical study identifies a class of ternary $Mg_xTM_{1-x}N$ ($TM = Ti, Zr, Hf, Nb$) nitrides that bridge these families. While these materials have rocksalt-derived crystal structures similar to binary $TMNs$, electronically they exhibit semiconducting band structures, large dielectric constants, and disorder-tunable properties. Lattice matching with main-group nitride semiconductors along some crystallographic orientations, and full structural compatibility with superconducting $TMNs$ make these materials uniquely poised for integration with established nitrides.

Author contributions: S.R.B., W.T., B.G., G.C., and A.Z. designed research; S.R.B., A.H., W.S., C.L.M., R.W.-R., J.M., J.P., A.T., and S.L. performed research; C.L.M. and A.T. contributed new reagents/analytic tools; S.R.B., A.H., W.S., J.M., J.P., S.L., and A.Z. analyzed data; and S.R.B., S.L., and A.Z. wrote the paper.

The authors declare no conflict of interest.

This article is a PNAS Direct Submission.

Published under the PNAS license.

Data deposition: Computational data available at National Renewable Energy Laboratory (NREL) MatDB: <https://materials.nrel.gov/>. Experimental data available at NREL HTEM DB: <https://hitem.nrel.gov/>.

¹To whom correspondence may be addressed. Email: sage.bauers@nrel.gov or andriy.zakutayev@nrel.gov.

This article contains supporting information online at www.pnas.org/lookup/suppl/doi:10.1073/pnas.1904926116/-DCSupplemental.

Published online July 3, 2019.

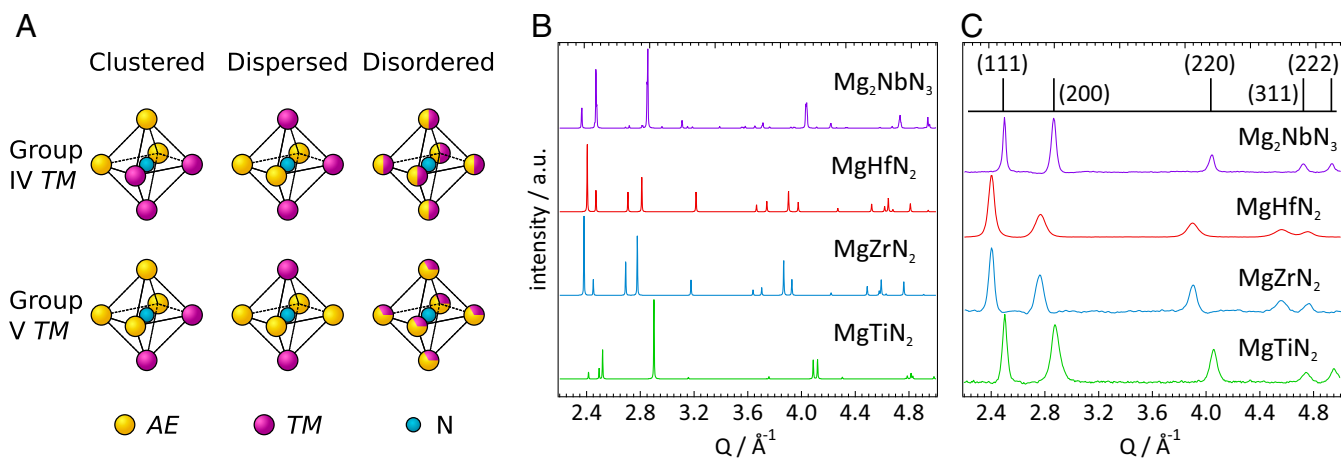


Fig. 1. Structural properties of $Mg_{G-3}TMN_{G-2}$ ($TM = Ti, Zr, Hf, Nb$) materials. (A) The charge-neutral local structural motifs that serve as building blocks for $AE_{G-3}TMN_{G-2}$ ($G = 4, 5$) rocksalt-derived structures. An alternative to the clustered and dispersed cation-ordered motifs is a substitutionally disordered cation lattice. (B) Calculated diffraction patterns for the rocksalt-derived ground states of $Mg_{G-3}TMN_{G-2}$ with an ordered cation sublattice. (C) Synchrotron X-ray diffraction data exhibit peaks that can be indexed to simple rocksalt (peak positions shown in black for $a = 4.46 \text{ \AA}$ to match Mg_2NbN_3), indicating the presence of substitutional disorder on the cation sublattice.

masses, and large dielectric constants (30 to 80 ϵ_0). Each of the compounds, synthesized as thin films via sputtering, exhibits diffraction peaks corresponding to a simple rocksalt structure and suggesting mixed cation-site occupancy. Lattice parameters are compatible with epitaxial growth on a variety of substrates and suitable for integration with well-established semiconducting and superconducting nitrides. Mg-rich compositions of $Mg_{G-3}TMN_{G-2}$ exhibit semiconducting electronic properties with visible-range optical absorption onsets, and electron mobilities approaching $100 \text{ cm}^2 \text{ V}^{-1} \cdot \text{s}^{-1}$ are measured from $MgZrN_2$ grown on MgO . Overall, these results introduce a class of ternary nitrides with semiconducting properties like main-group wurtzite nitrides, but rocksalt-derived crystal structures like superconducting $TMNs$.

Results

First, we hypothesize about possible structures found in $AE_{G-3}TMN_{G-2}$ rocksalt-derived nitrides for $G = 4$ and 5. The basis for any rocksalt-derived structure is octahedrally coordinated cations and anions forming a network of edge-sharing octahedra. In $AE_{G-3}TMN_{G-2}$ compounds only a few octahedral motifs will satisfy local electroneutrality, just like in the case of oxides (29). The motifs for $N-AE_3^{2+}TM_3^{4+}$ and $N-AE_4^{2+}TM_2^{5+}$ octahedra, corresponding to $AE^{2+}TM^{4+}N_2$ and $AE_2^{2+}TM^{5+}N_3$ stoichiometries, respectively, are shown in Fig. 1A. Each case has a clustered arrangement, where like cations are grouped together, and a dispersed arrangement, with like cations separated across the octahedron. Alternatively, in a disordered state the motifs can be mixed, and deviations from the ideal AE/TM ratio surrounding the N atoms may occur. However, this becomes energetically more costly the further they deviate from local charge neutrality, as recently shown for tetrahedrally coordinated ternary nitrides (30). Following the observed structural preferences in oxides and similar ternary nitrides, where radius ratio rules have been used to determine the coordination number and adopted motif (19, 21, 29), the smaller TM ions in $MgTiN_2$ are expected to promote clustered octahedral motifs, whereas $MgZrN_2$ and $MgHfN_2$ are expected to have dispersed motifs. Extending the same motif arguments to $AE_2^{2+}TM^{5+}N_3$ stoichiometries, Mg_2NbN_3 is expected to have a clustered $N-AE_4^{2+}TM_2^{5+}$ motif.

Our recent computational search for new ternary nitrides revealed several $AE-TM-N$ chemistries absent from the inorganic crystal structure database (9). To confirm our hypothetical considerations about the structures in the $Mg_{G-3}TMN_{G-2}$ family, we performed ab initio structure searches using the kinetically

limited minimization approach (11, 31). We obtained the layered α - $NaFeO_2$ structure [space group (SG) 166] for $MgTiN_2$ and the γ - $LiFeO_2$ structure (SG 141) for both $MgZrN_2$ and $MgHfN_2$. Each of these are rocksalt-derived structures, showing ABAB cation-site ordering perpendicular to $NaCl$ [111] planes for α - $NaFeO_2$, and parallel to both $NaCl$ [110] and $[-110]$ planes for γ - $LiFeO_2$. For Mg_2NbN_3 , the lowest energy is obtained for a 5-coordinate structure (SG 15). However, a rocksalt-derived structure (SG 12) is only 3.5 meV per atom higher in energy. Fig. 1B shows calculated X-ray diffraction patterns for these rocksalt-derived structures. Crystal structure schematics (SI Appendix, Fig. S1) and .cif files are provided in SI Appendix. For each system the lowest-energy rocksalt-derived structure exhibits local octahedral motifs as expected by the qualitative arguments above. However, our calculations show only a small energy penalty for adopting structures with different motifs (SI Appendix, Table S1), meaning these compounds can likely be disordered under nonequilibrium synthesis conditions.

To validate these predictions, we synthesized both stoichiometric ($x = 0$) and Mg-rich ($x \sim 0.5$) $Mg_{G-3+x}TM_{1-x}N_{G-2}$ ($TM = Ti, Zr, Nb, Hf$) thin films by combinatorial sputtering on glass substrates, with compositions summarized in Table 1. X-ray diffraction data for stoichiometric samples are shown in Fig. 1C. Diffraction from Mg-rich films (SI Appendix, Fig. S2) are similar, but relative peak intensities suggest different preferential orientation of the grains. Peak widths (SI Appendix, Table S2), indicate crystalline coherence lengths on the order of 10 nm, consistent with observations from transmission electron microscopy (TEM) micrographs from a $MgHfN_2$ lamella (SI Appendix, Fig. S3). TEM energy-dispersive X-ray spectroscopy measurements

Table 1. Target and measured compositions of Mg-TM-N thin films on glass substrates

Cation stoichiometric		Mg-rich	
Target	Measured	Target	Measured
$MgTiN_2$	$Mg_{0.97}TiN_{2.03}$	$Mg_{1.5}Ti_{0.5}N_2$	$Mg_{1.54}Ti_{0.46}N_{1.82}$
$MgZrN_2$	$Mg_{0.96}ZrN_{1.87}$	$Mg_{1.5}Zr_{0.5}N_2$	$Mg_{1.54}Zr_{0.46}N_{1.81}$
$MgHfN_2$	$Mg_{1.03}HfN_{2.21}$	$Mg_{1.5}Hf_{0.5}N_2$	$Mg_{1.52}Hf_{0.48}N_{1.88}$
Mg_2NbN_3	$Mg_{2.04}NbN_{2.78}$	$Mg_{2.5}Nb_{0.5}N_3$	$Mg_{2.46}Nb_{0.54}N_{2.47}$

Stoichiometric nitrogen measured from Mg-rich compositions is likely partially substituted by oxygen. Oxygen content measured from similar films deposited on C ranged from ~ 3 at % (stoichiometric) to ~ 7 at % (Mg-rich).

also support the absence of amorphous Mg_3N_2 or HfN in the film. For each *TM* the peaks can be indexed to a simple NaCl-type rocksalt structure (SG 225), with reference positions shown at the top for $a = 4.46 \text{ \AA}$. The lack of additional reflections, which would be present for the rocksalt-derived ground-state structures (Fig. 1B), suggest substitutional disorder on the cation lattice. This is not surprising given the similar ionic radii of Mg (0.86 Å) and the *TMs* (0.75 to 0.85 Å) (32), the prevalence of cation disorder in closed-shell oxide rocksalts (33), and the similar formation energy of structures with different local motifs (SI Appendix, Table S1).

The experimental confirmation of rocksalt-derived materials reported here, along with the already known cation-disordered ternary nitrides in wurtzite-derived crystal structures (11–13), suggests opportunities for future materials design with other “host” crystal structures. By considering additional materials, especially with structures known to accommodate substoichiometric defect phases (e.g., CsCl type, CaF_2 type), and elements that have capacity for redox stabilization by the inductive effect (e.g., *TMs*), it is likely that additional compounds with tunable properties can be realized. This design principle might extend beyond 4-coordinate wurtzites and 6-coordinate rocksalts, since some *TMNs* can adopt structures with up to 8-coordinate bonding, depending on composition (16, 34).

Next, we report measured optical and electronic properties of $Mg_{G-3+x}TM_{1-x}N_{G-2}$ thin films (Fig. 2). The cation-stoichiometric films prepared for this study had conductivities $>1 \text{ S cm}^{-1}$ and did not exhibit clearly defined optical absorption onsets, presumably due to degenerate carrier densities. Following the strategy of preparing $ZnSnN_2$ with low carrier densities by making it Zn-rich (35), we prepared Mg-rich compositions of $Mg_{G-3+x}TM_{1-x}N_{G-2}$ ($x \sim 0.5$). As presented in Fig. 2A, each Mg-rich composition exhibits an absorption onset (defined here as $\alpha = 10^4 \text{ cm}^{-1}$) in the visible range (1.8 to 2.1 eV) with $E_{Zr} \sim E_{Hf} < E_{Ti} < E_{Nb}$. Our experimental results agree with recent reports on $MgTiN_2$ and $MgZrN_2$, where a metallic-to-semiconducting transition is observed as Mg is added to *TMN* (27, 28).

Variable-temperature resistivity measurements from Mg-rich films are presented as an Arrhenius plot in Fig. 2B. The increase in resistivity with decreasing temperature is slightly weaker than exponential, indicating thermally activated transport is convoluted either with temperature-dependent mobility or other extrinsic factors. The calculated activation energy of the Zr-containing sample is 120 meV, suggesting the presence of a shallow defect. Room-temperature resistivities are significantly higher than at stoichiometric compositions, confirming that extrinsic carriers are

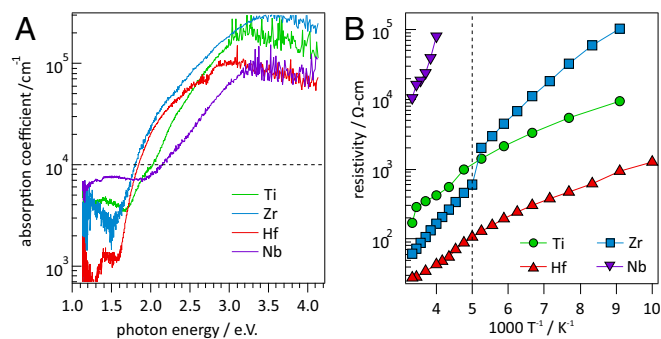


Fig. 2. Measured optical and electronic properties of Mg-rich $Mg_{G-3+x}TM_{1-x}N_{G-2}$ materials. (A) Experimental optical absorption spectra exhibit absorption onsets in the visible range. The horizontal dashed line indicates absorptivity of 10^4 cm^{-1} . (B) Semiconducting behavior is supported by an exponential increase in resistivity with decreasing temperature. The vertical dashed line indicates a switch in measurement conditions at $\sim 200 \text{ K}$.

Table 2. Transport properties of $MgZrN_2$ grown on MgO substrates

Substrate	$\rho, \Omega\text{-cm}$	$\mu, \text{cm}^2 \text{V}^{-1}\text{s}^{-1}$	n, cm^{-3}
(111) MgO	0.0192	90 ± 60	$(-5 \pm 3) \times 10^{18}$
(100) MgO	0.00118	42 ± 9	$(-1.3 \pm 0.3) \times 10^{20}$

Error is SD from 3 measurements.

partially compensated in Mg-rich films. Negative Seebeck voltages measured from $MgZrN_2$ films on glass substrates show n-type transport, likely from uncompensated oxygen acting as electron donors ($\sim 3\text{--}7 \%$ for witness samples on C substrates). Preliminary Hall effect experiments indicate that $MgZrN_2$ films grown by sputtering on MgO [similar to ScN epitaxy (36–38)] have mobilities approaching $100 \text{ cm}^2 \text{V}^{-1}\text{s}^{-1}$ (Table 2), which is very promising for a sputtered material.

To support these experimental property measurements, we computed electronic structure and resulting properties of $Mg_{G-3}TMN_{G-2}$ materials using many-body perturbation theory in the GW approximation (where G is the Green’s function and W is the screened Coulomb interaction) (39). The calculation results are summarized in Table 3. Electronic bandgaps of the rocksalt-derived structures are between 1 and 2 eV. The optical absorption (shown in Fig. 3B for $MgZrN_2$), exhibits a slow onset, nearly 1 eV above the bandgap, due to the indirect/forbidden nature of the optical transition (compare SI Appendix, Fig. S4 for other $Mg_{G-3}TMN_{G-2}$ compounds and for comparison with experiment). Notably, we obtain very large dielectric constants of 30 to 80 ϵ_0 , where ϵ_0 is vacuum permittivity, similar to the case of halide perovskites (40). This is likely because the d^0 configuration of the *TM* cations allows for large cation displacements at minute energy cost, thereby leading to a large ionic contribution to the dielectric constant (33). The electron and hole DOS effective masses (derived from density of states calculations) are between 0.6 and 1.9 m_0 (Table 3) which is comparable to Si (41), and is likely overestimated compared with $E(k)$ effective masses (derived from band structure calculations) due to degeneracy and/or nonparabolicity in the bands.

To understand the effects of cation-site disorder on material properties, we performed Monte Carlo supercell calculations, using the effective temperature (T_{eff}) concept (42). Note that T_{eff} is used to quantify nonequilibrium disorder due to kinetic limitations during thin-film growth at low and moderate temperatures, and does not directly relate to the actual growth temperature. We considered both a moderate level of disorder ($T_{\text{eff}} \sim 2,000 \text{ K}$), common for oxides and nitrides (42, 43), and strong disorder ($T_{\text{eff}} \sim 10,000 \text{ K}$). Detailed energetics of the disordered structures are given in SI Appendix, Table S3. The fraction of octet-violating polyhedra has been useful for describing disorder in tetrahedrally coordinated ternary nitrides (30, 44, 45). We take a similar approach and Fig. 3A shows the fraction of motifs found in the disordered structures of $MgZrN_2$. With moderate disorder almost 50% of octahedra have octet-rule-violating motifs, which do not significantly increase at higher T_{eff} . This is possibly because octahedrally coordinated compounds can have both clustered and dispersed forms of charge-neutral motifs, so increased disorder could be reasonably accommodated without additional charged motifs.

Calculated absorption spectra in Fig. 3B suggest that disorder alleviates the selection rules, thereby bringing the absorption onset closer to the bandgap energy. Relative to tetrahedrally coordinated ternary nitrides (30, 43), bandgaps are less affected by moderate and even strong disorder [Table 3, $\Delta E_g = 0.1$ to 0.3 eV for $Mg_{G-3}TMN_{G-2}$ vs. $\Delta E_g = 0.6 \text{ eV}$ at $T_{\text{eff}} = 0 \text{ K}$ vs. 3,000 K for $ZnSnN_2$ (30)], despite considerable deviations from the ideal octet-rule-conserving motifs in disordered $Mg_{G-3}TMN_{G-2}$. The changes to the bandgaps and effective masses with disorder depend on the interplay between band dispersion and more

Table 3. Calculated properties of $Mg_{G-3}TMN_{G-2}$ materials

Compound	Disorder state	Gap type	E_g , eV	E_g^{opt} , eV	m_e^*/m_0	m_h^*/m_0	ϵ_i/ϵ_0	ϵ_e/ϵ_0
MgTiN ₂	Ground state	Indirect	0.91	2.1	1.4	1.4	71.4	8.4
	Moderate-dis	NA	0.92	1.2	1.4	1.4		
	Strong-dis	NA	0.81	1.0	1.5	1.5		
MgZrN ₂	Ground state	Direct forbidden	1.47	2.5	0.6	1.6	31.6	6.9
	Moderate-dis	NA	1.67	2.2	1.1	2.1		
	Strong-dis	NA	1.39	1.8	1.3	2.4		
MgHfN ₂	Ground state	Direct forbidden	1.79	2.9	0.6	1.5	25.6	6.3
	Moderate-dis	NA	1.92	2.6	0.8	2.0		
	Strong-dis	NA	1.79	2.4	1.1	2.1		
Mg ₂ NbN ₃	Ground state	Indirect	1.84	2.7	0.6	1.9	61.0	7.1
	Moderate-dis	NA	2.14	2.3	1.5	3.6		
	Strong-dis	NA	1.66	1.8	1.3	3.7		

Electronic bandgap types, electronic bandgaps, optical absorption onsets (E_g^{opt} , defined as energy when $\alpha = 10^3 \text{ cm}^{-1}$), DOS effective masses, and dielectric constants (ϵ_i = ionic, ϵ_e = electronic). In disordered materials, the gap is not well defined (NA, not applicable).

localized perturbations and can be nonmonotonic (e.g., one would expect E_g to close in the limit $T_{eff} \rightarrow \infty$). We also note that disorder stabilizes the rocksalt-like structure of Mg_2NbN_3 over the distorted hexagonal structure of the ordered ground state (compare *SI Appendix, Table S3*), consistent with our observation of rocksalt in experiment.

To further examine the role of structural disorder on electronic properties of $Mg_{G-3}TMN_{G-2}$ compounds, we performed inverse participation ratio (IPR) calculations (46, 47) on ground state, moderately- and strongly-disordered $MgZrN_2$. Fig. 3C shows that the IPR of the ground-state structure is around 2 near the band edges, indicating about half the atoms contribute to these states, as is the case for many compound semiconductors. In the disordered materials, the magnitude of the IPR in the vicinity of the band edges is hardly affected, and no localized midgap states are observed. Thus, these IPR data indicate that $MgZrN_2$ and related semiconductors are electronically highly tolerant to disorder, even for the “worst-case” scenario of $T_{eff} = 10,000 \text{ K}$. The results are striking compared with tetrahedrally coordinated ternary nitrides, where already for $T_{eff} = 2,000 \text{ K}$ the IPR increased by over 2× at the valence band edge with a concomitant bandgap reduction by one-third (30). We attribute such “defect tolerance” (48, 49) to the exceptionally strong dielectric response in the rocksalt structure, where the potentially adverse effects of breaking the local octet rule are largely screened out.

The calculated structural, electronic, and optical properties of the $Mg_{G-3}TMN_{G-2}$ rocksalt materials are summarized in Fig. 4. As inspired by “bandgap engineering” (50) in zincblende and wurtzite compound semiconductors, Fig. 4A shows bandgap vs. effective lattice parameter for the rocksalt-derived crystal structures of $Mg_{G-3}TMN_{G-2}$ in comparison with related nitrides (51, 52). Also included is Mg_2TaN_3 , which was not experimentally investigated in this study, but is predicted to form in the same rocksalt-derived structure as Mg_2NbN_3 (*SI Appendix, Table S1*). The group-III *TMN* rocksalts and heterovalent $AE_{G-3}TMN_{G-2}$ rocksalts contain several compounds with a bandgap range of ~1 to 2 eV. These ternary rocksalt nitrides have effective cubic lattice parameters between 4.3 and 5.0 Å and effective hexagonal lattice parameters ($a_{cubic}/\sqrt{2}$) of 3.0 to 3.5 Å. Since *TM-N* rocksalts with a similar span of lattice parameters are known to form as ternary alloys and superlattices (36, 53), we postulate that similar materials could be made from *AE-TM-N* compounds. The hexagonal projection of $Mg_{G-3}TMN_{G-2}$ lattice parameters also falls within the range of InN-GaN-AlN *a*-lattice parameters.

Fig. 4B shows a color map of optical absorption onsets ($\alpha = 10^3 \text{ cm}^{-1}$) for $Mg_{G-3}TMN_{G-2}$ with contour lines indicating electron effective masses, both as a function of effective temperature and lattice parameter. The 2D linear interpolation is generated from the calculated values highlighted by white hexagons for ground-state, moderately disordered, and strongly disordered structures. Even though disorder only marginally affects the

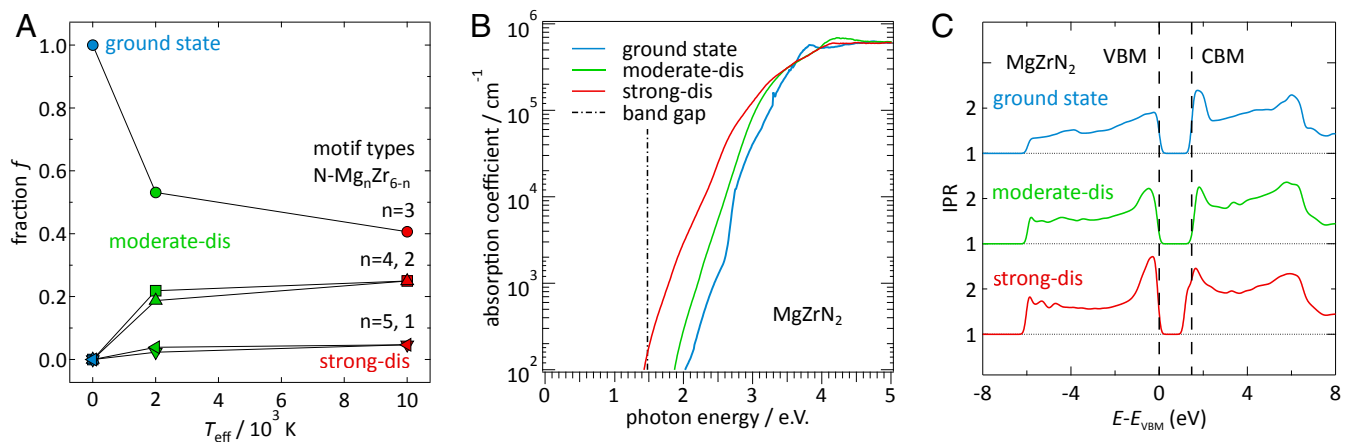


Fig. 3. Calculated properties of $MgZrN_2$. (A) Fraction of octet-rule-violating motifs as a function of effective temperature. (B) Optical absorption spectra and bandgap for the rocksalt-derived ground-state structure, and absorption of moderately (moderate-dis) and strongly (strong-dis) disordered structures. (C) IPR data show that carrier localization and bandgap change negligibly with disorder.

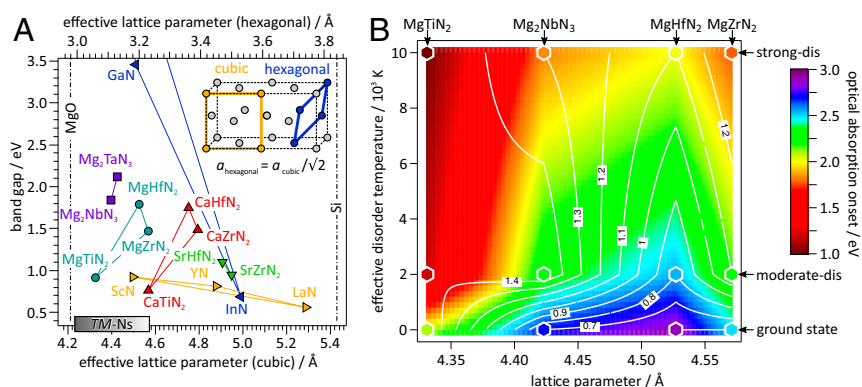


Fig. 4. Tunable properties of $Mg_{G-3}TMN_{G-2}$ semiconductors. (A) Bandgap vs. effective lattice parameter for $Mg_{G-3}TMN_{G-2}$, group-III nitrides, other AE-TM-N₂ materials, and Si/MgO substrates (51, 52). (B) Interpolation of optical absorption onset (color) and electron effective mass (contour lines) between different $Mg_{G-3}TMN_{G-2}$ lattice parameters and degrees of disorder, as indicated by effective temperature.

electronic bandgaps, absorption onsets systematically decrease in energy with disorder. Thus, the degree of disorder could be utilized to tune the absorption strength to the needs of an application without deteriorating charge-transport properties. Since the absorption onset is generally more sensitive to disorder than to lattice parameter, these “disorder-tuned” materials might also be “structurally tuned” to the desired lattice constant via TM alloying.

Finally, we speculate about potential future applications of the $Mg_{G-3}TMN_{G-2}$ materials reported here. The coexistence of multiple useful phenomena, such as superconducting and semiconducting properties, is a key feature of metal nitrides. For example, structural compatibility between (111) NbN and (001) GaN was recently demonstrated in epitaxial heterostructures with a 2D electron gas in GaN and superconductivity in NbN (54). These $Mg_{G-3}TMN_{G-2}$ materials, which are structurally compatible with both III-N semiconductors and TM-N superconductors, will allow for such types of integration. In particular, semiconductor/superconductor heterojunctions with complete structural and chemical compatibility across $Mg_{G-3}TMN_{G-2}/TMN$ interfaces might be achievable. Such high-quality interfaces, with defect-tolerant high-k $Mg_{G-3}TMN_{G-2}$ barriers, might enable low-loss Josephson junctions for next-generation quantum computers (55, 56) and other emerging applications.

In conclusion, we have introduced a family of $Mg_{G-3}TMN_{G-2}$ ($TM = Ti, Zr, Nb, Hf$) semiconducting materials with rocksalt-derived crystal structures, and studied their optical and electronic properties using both sputtered thin-film experiments and ab initio calculations. For each studied material, the measured diffraction patterns are consistent with the calculated rocksalt-derived structures, but with significant antisite disorder on the cation sublattice. When the materials are synthesized with Mg-rich stoichiometry, they exhibit semiconducting properties, including temperature-activated electrical conductivity and optical absorption onsets in the visible range. Ab initio calculations suggest that the optical absorption onset can be tuned both by choice of TM and the degree of ordering on the cation sublattice, while the bandgaps and effective masses exhibit a remarkable tolerance to structural cation disorder. These rocksalt semiconductors may be a subset of a larger family of chemically intuitive compounds formed from host materials containing TMs in structures known to accommodate off-stoichiometric defect phases. This suggests opportunities for design of defect-tolerant

semiconductors outside of the familiar space of main-group tetrahedrally bonded materials. The potential for integrating these $Mg_{G-3}TMN_{G-2}$ rocksalt nitrides into semiconductor/superconductor heterostructure devices is highlighted by their structural compatibility with several existing nitrides, and by the promising transport properties measured from sputtered epitaxial films.

Methods

Thin films were grown by radiofrequency sputtering from elemental targets onto glass substrates at a deposition temperature of 400 °C. A gas cracker was used to increase nitrogen reactivity. These films were analyzed for structure via X-ray diffraction at the Stanford Synchrotron Radiation Lightsource (SSRL) and for composition using Rutherford backscattering spectrometry. Electronic transport and optical properties were determined by resistivity and Hall measurements in a van der Pauw geometry, and UV-visible spectroscopy, respectively. Experimental data used by this study have been analyzed using the COMBitor software package (57) and are publicly available in the [National Renewable Energy Laboratory \(NREL\)](https://nrel.gov) high-throughput experimental materials database at <https://hitem.nrel.gov> (58).

First-principles density-functional and many-body perturbation theory calculations were performed with the VASP code, employing the generalized gradient and GW approximations, respectively (59, 60). The ground-state structure search was performed using the “kinetically limited minimization” approach, which is unconstrained and does not require prototypical structures from databases (11). Disordered structures were generated through first-principles Monte Carlo sampling in supercells between 64 and 96 atoms (5 random seeds per each case) using the Metropolis criterion for 2,000 and 10,000 K as effective temperature (42) for moderate and strong disorder, respectively. To calculate the electronic structure and optical absorption for these supercells, we used the single-shot-hybrid plus onsite potential approach (30, 51), with parameters fitted to the GW calculations of the ground states (SI Appendix, Table S4). More detailed information regarding the materials and methods are available in the SI Appendix.

ACKNOWLEDGMENTS. This work was supported by the U.S. Department of Energy (DOE) under Contract DE-AC36-08GO28308 with Alliance for Sustainable Energy, LLC, the Manager and Operator of the NREL. Funding provided by Office of Science (SC), Office of Basic Energy Sciences (BES), as part of the Energy Frontier Research Center “Center for Next Generation of Materials Design: Incorporating Metastability.” High-performance computing resources were sponsored by the DOE, Office of Energy Efficiency and Renewable Energy. Use of the SSRL, SLAC National Accelerator Laboratory, was supported by the DOE, SC, BES under Contract DE-AC02-76SF00515. Work by A.T. and C.M. was supported by the DOE, SC, BES, Materials Sciences and Engineering Division. We thank Dr. Suchismita Sarker and Dr. Apurva Mehta for assistance at SLAC BL1-5.

1. F. Ponce, D. P. Bour, Nitride-based semiconductors for blue and green light emitting devices. *Nature* **386**, 351–359 (1997).
2. U. K. Mishra, P. Parikh, Y.-F. Wu, AlGaN/GaN HEMTs—an overview of device operation and applications. *Proc. IEEE* **90**, 1022–1031 (2002).
3. S. Nakamura, The roles of structural imperfections in InGaN-based blue light-emitting diodes and laser diodes. *Science* **281**, 955–961 (1998).

4. M. Wittmer, Properties and microelectronic applications of thin films of refractory metal nitrides. *J. Vac. Sci. Technol. A* **3**, 1797–1803 (1985).
5. X.-J. Chen et al., Hard superconducting nitrides. *Proc. Natl. Acad. Sci. U.S.A.* **102**, 3198–3201 (2005).
6. A. K. Tareen, G. S. Priyanga, S. Behara, T. Thomas, M. Yang, Mixed ternary transition metal nitrides: A comprehensive review of synthesis, electronic

- structure, and properties of engineering relevance. *Prog. Solid State Chem.* **53**, 1–26 (2019).
7. A. Miura *et al.*, Octahedral and trigonal-prismatic coordination preferences in Nb-, Mo-, Ta-, and W-based ABX₂ layered oxides, oxynitrides, and nitrides. *J. Solid State Chem.* **229**, 272–277 (2015).
 8. Y. Hinuma *et al.*, Discovery of earth-abundant nitride semiconductors by computational screening and high-pressure synthesis. *Nat. Commun.* **7**, 11962 (2016).
 9. W. Sun *et al.*, A map of the inorganic ternary metal nitrides. *Nat. Mater.* **18**, 732–739 (2019).
 10. D. Gall *et al.*, Electronic structure of ScN determined using optical spectroscopy, photoemission, and *ab initio* calculations. *Phys. Rev. B* **63**, 125119 (2001).
 11. E. Arca *et al.*, Redox-mediated stabilization in zinc molybdenum nitrides. *J. Am. Chem. Soc.* **140**, 4293–4301 (2018).
 12. A. D. Martinez, A. N. Fioretti, E. S. Toberer, A. C. Tamboli, Synthesis, structure, and optoelectronic properties of II-IV-V₂ materials. *J. Mater. Chem. A* **5**, 11418–11435 (2017).
 13. E. Arca *et al.*, Zn₂SbN₃: Growth and characterization of a metastable photoactive semiconductor. *Mater. Horiz.* **10**, 1039/C9MH00369J (2019).
 14. D. H. Gregory, Structural families in nitride chemistry. *J. Chem. Soc. Dalton Trans.*, **1999**, 259–270 (1999).
 15. J. Etourneau, J. Portier, F. Ménéil, The role of the inductive effect in solid state chemistry: How the chemist can use it to modify both the structural and the physical properties of the materials. *J. Alloys Compd.* **188**, 1–7 (1992).
 16. L. Toth, *Transition Metal Carbides and Nitrides* (Elsevier Science, 1971).
 17. A. W. Jackson, O. Shebanova, A. L. Hector, P. F. McMillan, Amorphous and nanocrystalline titanium nitride and carbonitride materials obtained by solution phase ammonolysis of Ti(NMe₂)₄. *J. Solid State Chem.* **179**, 1383–1393 (2006).
 18. V. S. Bhadram *et al.*, Semiconducting cubic titanium nitride in the Th₃P₄ structure. *Phys. Rev. Mater.* **2**, 011602 (2018).
 19. E. Orisakwe, B. Fontaine, D. H. Gregory, R. Gautier, J.-F. Halet, Theoretical study on the structural, electronic and physical properties of layered alkaline-earth-group-4 transition-metal nitrides AEMN₂. *RSC Adv.* **4**, 31981–31987 (2014).
 20. M. A. Gharavi, R. Armiento, B. Alling, P. Eklund, Theoretical study of phase stability, crystal and electronic structure of MeMgN₂ (Me = Ti, Zr, Hf) compounds. *J. Mater. Sci.* **53**, 4294–4305 (2018).
 21. D. H. Gregory, M. G. Barker, P. P. Edwards, D. J. Siddons, Synthesis and structure of two new layered ternary nitrides, SrZrN₂ and SrHfN₂. *Inorg. Chem.* **35**, 7608–7613 (1996).
 22. D. H. Gregory, M. G. Barker, P. P. Edwards, M. Slaski, D. J. Siddons, Synthesis, structure, and magnetic properties of the new ternary nitride BaHfN₂ and of the BaHf_{1-x}Zr_xN₂ Solid solution. *J. Solid State Chem.* **137**, 62–70 (1998).
 23. D. H. Gregory, M. G. Barker, P. P. Edwards, D. J. Siddons, Synthesis and structure of the new ternary nitride SrTiN₂. *Inorg. Chem.* **37**, 3775–3778 (1998).
 24. T. Brokamp, H. Jacobs, Darstellung und Struktur einiger Gemischtvalenter ternärer tantalnitride mit lithium und magnesium. *J. Alloys Compd.* **183**, 325–344 (1992).
 25. M. Fenker, M. Balzer, H. Kappel, O. Banakh, Some properties of (Ti,Mg)N thin films deposited by reactive dc magnetron sputtering. *Surf. Coat. Technol.* **200**, 227–231 (2005).
 26. B. Alling, Metal to semiconductor transition and phase stability of Ti_{1-x}Mg_xN_y alloys investigated by first-principles calculations. *Phys. Rev. B* **89**, 085112 (2014).
 27. B. Wang *et al.*, Growth and properties of epitaxial Ti_{1-x}Mg_xN (001) layers. *J. Vac. Sci. Technol. A* **36**, 061501 (2018).
 28. S. R. Bauers *et al.*, Composition, structure, and semiconducting properties of Mg_xZr_{2-x}N₂ thin films. *Jpn. J. Appl. Phys.* **58**, SC1015 (2019).
 29. G. C. Mather, C. Dussarrat, J. Etourneau, A. R. West, A review of cation-ordered rock salt superstructure oxides. *J. Mater. Chem.* **10**, 2219–2230 (2000).
 30. S. Lany *et al.*, Monte Carlo simulations of disorder in ZnSnN₂ and the effects on the electronic structure. *Phys. Rev. Mater.* **1**, 035401 (2017).
 31. P. P. Zawadzki, J. Perkins, S. Lany, Modeling amorphous thin films: Kinetically limited minimization. *Phys. Rev. B* **90**, 94203 (2014).
 32. R. D. Shannon, I. U. Cr, Revised effective ionic radii and systematic studies of interatomic distances in halides and chalcogenides. *Acta Crystallogr. A* **32**, 751–767 (1976).
 33. A. Urban, A. Abdellahi, S. Dacek, N. Artrith, G. Ceder, Electronic-structure origin of cation disorder in transition-metal oxides. *Phys. Rev. Lett.* **119**, 176402 (2017).
 34. A. Salamat, P. Kroll, P. F. McMillan, Nitrogen-rich transition metal nitrides. *Coord. Chem. Rev.* **257**, 2063–2072 (2013).
 35. A. N. Fioretti *et al.*, Combinatorial insights into doping control and transport properties of zinc tin nitride. *J. Mater. Chem. C* **3**, 11017–11028 (2015).
 36. B. Saha, A. Shakouri, T. D. Sands, Rocksalt nitride metal/semiconductor superlattices: A new class of artificially structured materials. *Appl. Phys. Rev.* **5**, 021101 (2018).
 37. M. A. Moram, Y. Zhang, M. J. Kappers, Z. H. Barber, C. J. Humphreys, Dislocation reduction in gallium nitride films using scandium nitride interlayers. *Appl. Phys. Lett.* **91**, 152101 (2007).
 38. M. A. Moram *et al.*, Growth of epitaxial thin films of scandium nitride on 100-oriented silicon. *J. Cryst. Growth* **310**, 2746–2750 (2008).
 39. L. Hedin, New method for calculating the one-particle green's function with application to the electron-gas problem. *Phys. Rev.* **139**, A796–A823 (1965).
 40. I. Anusca *et al.*, Dielectric response: Answer to many questions in the methylammonium lead halide solar cell absorbers. *Adv. Energy Mater.* **7**, 1700600 (2017).
 41. M. A. Green, Intrinsic concentration, effective densities of states, and effective mass in silicon. *J. Appl. Phys.* **67**, 2944–2954 (1990).
 42. P. F. Ndione *et al.*, Control of the electrical properties in spinel oxides by manipulating the cation disorder. *Adv. Funct. Mater.* **24**, 610–618 (2014).
 43. A. N. Fioretti *et al.*, Exciton photoluminescence and benign defect complex formation in zinc tin nitride. *Mater. Horiz.* **5**, 823–830 (2018).
 44. P. C. Quayle *et al.*, Charge-neutral disorder and polytypes in heterovalent wurtzite-based ternary semiconductors: The importance of the octet rule. *Phys. Rev. B* **91**, 205207 (2015).
 45. D. Skachkov, P. C. Quayle, K. Kash, W. R. L. Lambrecht, Disorder effects on the band structure of ZnGeN₂: Role of exchange defects. *Phys. Rev. B* **94**, 205201 (2016).
 46. L. L. Baranowski *et al.*, Effects of disorder on carrier transport in Cu₂SnS₃. *Phys. Rev. Appl.* **4**, 044017 (2015).
 47. P. Zawadzki, A. Zakutayev, S. Lany, Entropy-driven clustering in tetrahedrally bonded multinary materials. *Phys. Rev. Appl.* **3**, 034007 (2015).
 48. R. E. Brandt, V. Stevanović, D. S. Ginley, T. Buonassisi, Identifying defect-tolerant semiconductors with high minority-carrier lifetimes: Beyond hybrid lead halide perovskites. *MRS Commun.* **5**, 265–275 (2015).
 49. A. Zakutayev *et al.*, Defect tolerant semiconductors for solar energy conversion. *J. Phys. Chem. Lett.* **5**, 1117–1125 (2014).
 50. I. Vurgaftman, J. R. Meyer, L. R. Ram-Mohan, Band parameters for III–V compound semiconductors and their alloys. *J. Appl. Phys.* **89**, 5815–5875 (2001).
 51. S. Lany, Band-structure calculations for the 3d transition metal oxides in GW. *Phys. Rev. B* **87**, 085112 (2013).
 52. J. Wu *et al.*, Temperature dependence of the fundamental band gap of InN. *J. Appl. Phys.* **94**, 4457–4460 (2003).
 53. G. M. Matenoglou *et al.*, Structure, stability and bonding of ternary transition metal nitrides. *Surf. Coat. Tech.* **204**, 911–914 (2009).
 54. R. Yan *et al.*, GaN/NbN epitaxial semiconductor/superconductor heterostructures. *Nature* **555**, 183–189 (2018).
 55. V. Mourik *et al.*, Signatures of Majorana fermions in hybrid superconductor-semiconductor nanowire devices. *Science* **336**, 1003–1007 (2012).
 56. W. D. Oliver, P. B. Welander, Materials in superconducting quantum bits. *MRS Bull.* **38**, 816–825 (2013).
 57. K. R. Talley *et al.*, COMBigor: Data analysis package for combinatorial materials science. *ACS Comb. Sci.* **10**, 1021/acscombsci.9b00077 (2019).
 58. A. Zakutayev *et al.*, An open experimental database for exploring inorganic materials. *Sci. Data* **5**, 180053 (2018).
 59. G. Kresse, D. Joubert, From ultrasoft pseudopotentials to the projector augmented-wave method. *Phys. Rev. B* **59**, 1758–1775 (1999).
 60. M. Shishkin, G. Kresse, Implementation and performance of the frequency-dependent GW method within the PAW framework. *Phys. Rev. B* **74**, 035101 (2006).